JOURNAL OF GEOPHYSICAL RESEARCH, VOL. 104, NO. 12, PAGES 28,789–28,802, DECEMBER 10, 1999

Slab temperature and thickness from seismic tomography 1. Method and application to Tonga

Michael M. Deal[1] and Guust Nolet
Department of Geosciences, Princeton University, Princeton, New Jersey

Rob D. van der Hilst
Department of Earth, Atmospheric and Planetary Sciences, Massachusetts Institute of Technology, Cambridge

Abstract. Delay times of compressional body wave phases from both teleseismic and local events are used to invert for a high-resolution P wave velocity model in the Tonga subduction zone. The images obtained show a high-velocity subducting slab with velocity deviations of the order of 3–4%. Assuming to first order that the positive velocity anomalies within the slab are caused by a temperature effect, a theoretical slab temperature model based on the diffusion equation is used to explain velocity anomalies within the tomographic slab. Temperature differences between the interior of the slab and the ambient mantle are converted to velocity perturbations using the scaling parameter $dV_p/dT \approx 4.8 \times 10^{-4}$ km s^{-1} °C^{-1} for lithosphere material. The optimal values for the parameters in the temperature model are found using a nonlinear optimization that compares the integrated velocity anomalies in the tomographic slab region to integral of high velocities in a synthetic slab derived from a temperature model. The parameters for slab thickness and mantle potential temperature are not uniquely determined; therefore a fixed value for the mantle potential temperature based on laboratory values for the temperature of the spinel-to-perovskite transition at 660 km is used. Using 1180°C as the potential temperature, the theoretical temperature model gives an optimal slab thickness of 82 km for a region near 29°S in Tonga. The uncertainty in the thickness is dominated by the uncertainty in the mantle temperature and would be 8 km for an uncertainty of 100° in mantle temperature, but nonsystematic errors are less. In order to enhance the tomographic result the velocity model is biased towards the theoretical slab model. However, a posteriori changes made to the tomogram will most likely violate the fit to the delay time data. To prevent this, the difference between the tomogram and the predicted slab model is projected onto the null-space of the inversion to remove components which do not satisfy the seismic data. Using only null-space components to modify the minimum-norm solution, an enhanced model is obtained which has been biased toward the theoretical solution but has the same data misfit as the minimum-norm solution. The final image shows a very narrow and continuous slab with maximum velocity anomalies of the order of 6–7%; many of the gaps within the slab, as well as artifacts around the slab which were present in the minimum-norm solution, are absent in the biased image.

1. Introduction

Since its conception three decades ago, the theory of plate tectonics has led Earth scientists to redefine their understanding of the dynamics of the Earth. One of the most heavily studied facets of plate tectonics is convergent plate boundaries where subduction occurs. Subduction regions have become the focus of much attention for a number of diverse reasons. Not only are subduction zones responsible for the vast majority of deep focus earthquakes, they also represent one of the few situations where we can study the chemical and physical interaction between the mantle and the elastic lithosphere.

The first representation of subduction regions was provided through Wadati-Benioff zones which map the distribution of subduction zone earthquakes [*Wadati*, 1935; *Sykes*, 1966; *Oliver and Isacks*, 1967]; however, Benioff zones depict only the location of seismic strain within the slab and only where the stress is not relaxed by creep. Other evidence pertaining to slabs is derived from waveform analysis of subduction zone events [*Vidale*, 1987; *Zhou and Chen*, 1995], as well as from residual sphere analysis [*Creager and Jordan*, 1986; *Fischer et al.*, 1991]. Recently, the results of seismic tomography have provided glimpses of the Earth's interior structure. Previous tomographic studies of slabs confirmed dipping structures of high seismic velocities, which nicely overlaid Benioff zones [e.g., *Hirahara*, 1977; *Spakman et al.*, 1988; *Inoue et al.*, 1990; *Zhou and Clayton*, 1990; *van der Hilst et al.*, 1991; *Zhao et al.*, 1997]. These tomographic studies have provided a large amount of qualitative evidence supporting the theory of plate tectonics, but slab images have not yet been combined with theoretical modeling to invert for quantitative information about the physical state within the Earth. *de Jonge et al.*, [1994] used a forward modeling procedure to derive theoretical ve-

[1]Now at Exxon Production Research Company, Houston, Texas.

Paper number 1999JB900255.
0148-0227/99/1999JB900255$09.00

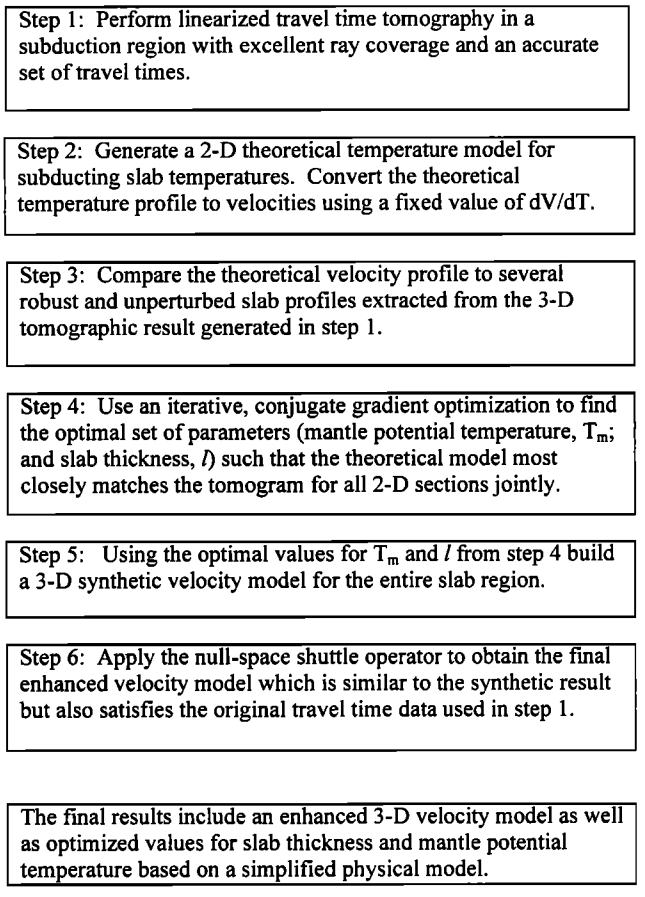

Figure 1. A flowchart depicting the basic steps taken in our procedure.

locity models for the upper mantle and lithosphere based on previous tectonic reconstructions and compared the synthetic velocity models to travel time tomograms. They did not use the synthetic models to enhance or modify the tomographic images. *Koper et al.* [1998] used forward modeling to investigate the possibility of an olivine wedge in the subducting slab.

Along with the seismological exploration of subduction regions, a number of workers have developed theoretical models to explain subduction mechanics as well as mantle convection, interactions between the lithosphere and the mantle, and petrology and chemistry of the mantle. These models are often used in conjunction with supporting experimental results to further our understanding of subduction. For example, *Fischer et al.* [1991] used the temperature model of *Toksoz et al.* [1971] along with residual sphere analysis to determine the vertical extent of the slab as well as a simple thermal structure of the slab.

In this study we unite a simple thermal model for subducting material with the results of a high-resolution, three-dimensional tomographic study of the Tonga-Fiji region. Our aim is twofold. First, we obtain acceptable values for the model parameters, such as mantle temperature and slab thickness, as well as a slab temperature profile. Unlike previous temperature profiles, our results are based on a direct fit of a physical model to tomographic images. We use seismic delay times to find the optimal values for the temperature model parameters as well as to confirm the theoretical model. The values of the physical parameters we obtain from the inversion of the temperature model can then be used along with mineral physics laboratory data to study the interaction between the slab and the mantle. For example, the interior temperature of the slab at the 400-km discontinuity is an important factor in determining the extent to which the phase change from olivine to spinel will be kinetically inhibited [*Rubie and Ross*, 1994]. The temperature structure of the slab is also crucial in determining the possibility that volatiles will be subducted into the transition zone [*Gasparik*, 1993; *Nolet and Zielhuis*, 1994]. Slab temperatures at the 660-km discontinuity can be used to help explain or infer the future of lithospheric material after it reaches the 660-km boundary [*van Keken et al.*, 1996].

Second, the use of a theoretical model for the slab enables us to substantially enhance the final tomographic image without affecting the data fit. We maintain an acceptable misfit by using only null-space components to bias the tomographic image in the direction of the theoretical temperature model [*Deal and Nolet*, 1996b]. The quality and resolution of previous tomographic studies of slabs have depended heavily on data quality as well as ray coverage. Poor data or inadequate ray coverage lead to artifacts and regions with low resolution. Owing to the underdetermined nature of the inverse problem, no unique solution exists. Our technique provides a method to incorporate additional information in the tomographic image without affecting the misfit. Essentially we reparametrize the slab portion of the velocity model using a theoretical temperature model; the result is a huge reduction in the number of parameters. If the changes to the velocity model (induced by the theoretical temperature model) can be projected onto the null-space, we conclude that the theoretical model and the new parametrization satisfy the seismic data.

We demonstrate the method and present results for the Tonga subduction region. In this study we combine tomography with a quantitative, theoretical temperature model for slab temperatures. A flowchart depicting the basic steps taken in our procedure is shown in Figure 1. We stress that the null-space projection operator, referred to as the "null-space shuttle," can be used with all linearized inverse problems which result in a singular or nearly singular matrix. Our procedure can easily be utilized in other settings where one wishes to test a theoretical model or to apply a priori knowledge to an inversion based on experimental data.

2. Tomographic Inversion

In order to compare a tomographic model to a theoretical temperature model it is necessary to obtain a high-resolution tomographic image of the velocity structure. The two major issues to address in order to achieve an adequate resolution are ray coverage and model parametrization. Many of the steps involved in the tomographic inversion are similar to those of *van der Hilst* [1995]. Here we will point out where we have made substantial improvements or modifications which are relevant for our purposes.

2.1. Data

In order to achieve excellent ray coverage we use various *P* wave phases reported to the International Seismological Centre (ISC) between 1967 and 1995. The data set, hereinafter referred to as EHB data, from which we choose our rays was compiled by *Engdahl et al.* [1998] and includes over one million data. The velocity model includes the region between 0.5°S and 50.0°S, and 170.0°E to 170.0°W, down to a depth of 1500 km,

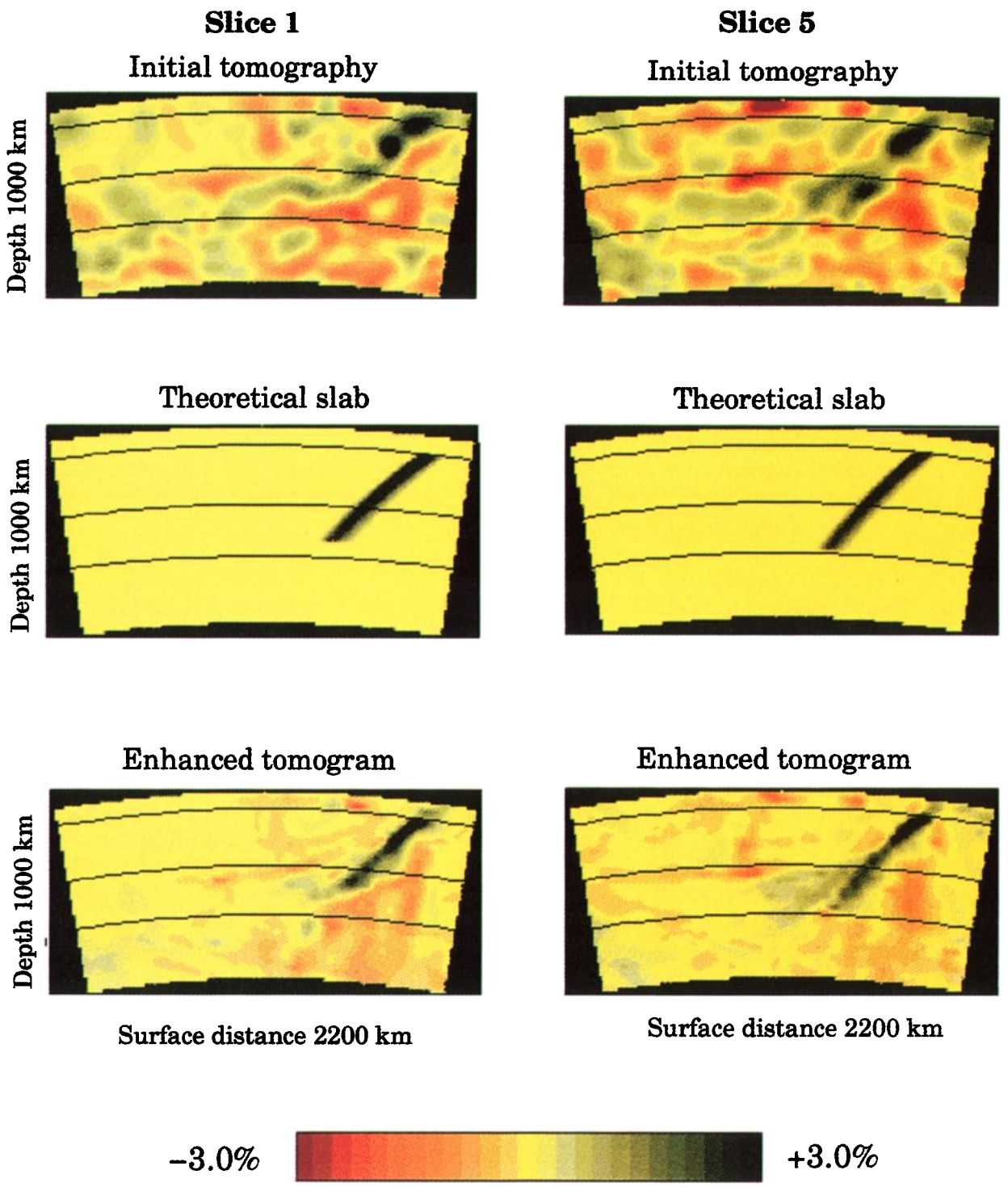

Plate 1. Two vertical slices through the velocity model depict the method used to enhance the tomographic images and determine optimal values for T_m and l. The two slices at the top of Plate 1 are from the initial tomographic model. In total, 16 slices at 0.5° increments are taken through the three-dimensional model from the region marked in Figure 3 (slice 1 to the north). The middle row in Plate 1 corresponds to the theoretical slab velocity model based on the optimal values (T_m = 1180°C, l = 82 km). The theoretical slab model has no velocity structure outside of the slab or below 660 km because the analytical model only specifies temperature deviations within the slab, above 660 km. The two slices in the bottom row in Plate 1 are the final result after projecting the difference between the theoretical model (middle row) and the original tomogram (top row) onto the null-space. The original tomographic result and the enhanced image both have nearly an identical misfit to the seismic travel times. The final images in the bottom row have been strongly biased in the direction of the theoretical slab model and only deviate from it as required by the seismic data.

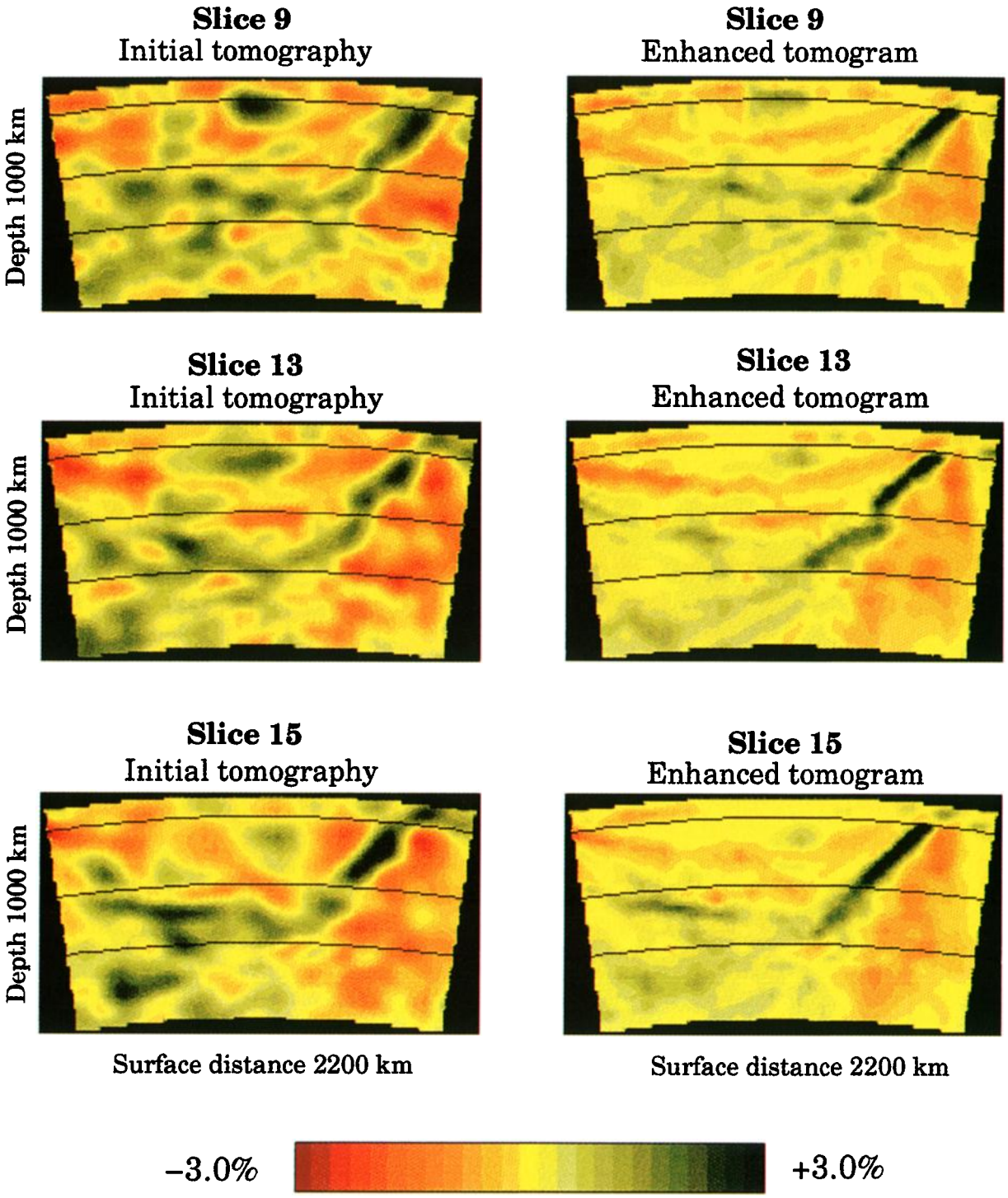

Plate 2. Three additional vertical slices through the velocity model. Slices on the left are extracted from the initial 3-D tomographic inversion. Slices on the right are the final images after the null-space projection. The final slices are taken from the enhanced 3-D solution that most closely resembles the theoretical slab model while still satisfying the seismic delay times. In the enhanced images the slab region appears to be more continuous and better defined than in the original minimum-norm tomographic solution.

and the rays chosen for the tomographic inversion are from events both within the velocity model and from teleseismic events outside of the region that are recorded by stations within the velocity model. The event hypocenters have been previously relocated using the method of *Engdahl et al.* [1998]. The relocation algorithm used by Engdahl et al. is an iterative procedure based on arrivals of prominent body waves, such as *P*, *pP*, and *S* arrivals; during the process, phase arrivals are reidentified based on a comparison to theoretical arrival times and robust statistics. Owing to the massive number of arrival times in the data set we are able to be selective in our choice of data and demand a certain level of quality. Specifically, we use only impulsive *P* wave arrivals that have a residual less than a prescribed threshold. The initial distribution of residuals after relocation, but prior to tomographic inversion, is shown in Figure 2. In order to reduce the model artifacts common in tomographic inversions we attempt to remove potential outliers. A simple calculation shows that a ray which travels up through the slab could very likely have a residual >3 s. Moreover, test inversions show that the perturbations in some regions were reduced significantly when we removed residuals with absolute values >3 s. We therefore chose a cut off value of 4.9 s, which is the 3σ level for the residuals (Figure 2). The residuals are all calculated with respect to the one-dimensional ak135 background Earth model [*Kennett et al.*, 1995] and are corrected for the Earth's ellipticity. A correction is also made for the bounce point elevation for all reflected phases as well as station elevation [*Engdahl et al.*, 1998]. Our final data set consists of over 350,000 rays, and includes *P*, *PP*, *PKP*, and *PKIKP* as well as *pP*.

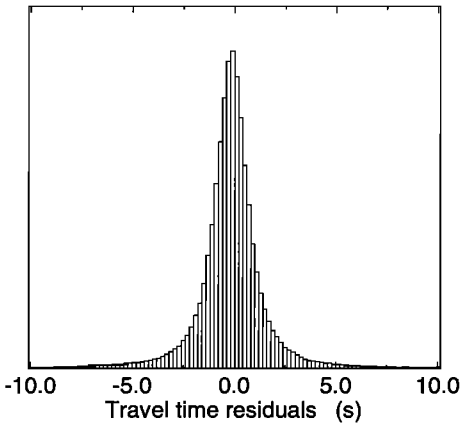

Figure 2. Histogram of the initial distribution of EHB delay times after the hypocentral relocation procedure of *Engdahl et al.* [1998] but prior to the tomographic inversion. The value for 3σ is 4.9 s; using a cutoff much less than this causes a loss in amplitudes of the velocity anomalies.

2.2. Model Parametrization

In order to achieve a high resolution in the region of the subduction zone we parametrize the model using a three-dimensional Cartesian grid of nodes spaced 50 km in the x and y directions and 30 km in the z direction (approximate depth). Trilinear interpolation is used to calculate the velocity perturbation between nodes. Previous studies have often been based on a constant velocity cell parametrization. However, for our purposes, this proved unacceptable since the rapid changes in velocity in a subduction region render a parametrization based on cells with constant velocity inadequate. The close spacing of our nodes represents a substantial improvement over many previous studies. More recent inversions such as by *Zhao et al.* [1997] have also had tremendous success using a closely spaced parameterization. Comparing our results to those using a more coarse parametrization, we see the same major features, although the amplitudes, as well as the amount of fine scale detail, are increased by using closely spaced nodes. For example, *van der Hilst* [1995] shows the Tonga slab as several distinct high-velocity patches. Our initial tomographic results (Plates 1 and 2) link the high velocity regions seen by *van der Hilst* [1995] into a much more continuous, narrower feature. Besides using more closely spaced nodes, we also include a smoothing matrix (equation (2)), while *van der Hilst* [1995] used norm damping.

The area of interest is the Tonga trench and the region beneath the South Fiji Basin. However, the velocity model consists of an area somewhat larger than the immediate Tonga region in order to avoid any edge-related phenomenon from affecting the slab and its immediate vicinity (see Figure 3). The model has ~500,000 velocity nodes as well as 7000 parameters for station corrections and parameters for 80,000 event relocations. Hypocentral relocation parameters are included in the inversion to account for possible heterogeneities outside of the model; they are not meant to be an improvement to those of *Engdahl et al.* [1998]. Small station corrections are also permitted in the inversion. For reasons of computational efficiency the model is parametrized as a Cartesian grid of nodes; since the Earth is spherical, a portion of the nodes lie outside of the Earth and remain unaffected by the inversion.

2.3. Travel Time Inversion

We use the LSQR algorithm for the inversion of the travel time residuals for velocity perturbations, station corrections, and hypocentral relocations. LSQR is an iterative, conjugate gradient method that quickly converges to the least squares solution. Minimizing the Euclidean norm of the misfit vector is theoretically not the ideal choice but is usually chosen for its speed and ease of implementation. In choosing the least squares solution we have assumed that the delay time errors (including modeling errors) follow a normal distribution. In matrix notation the tomographic inverse problem is

$$\mathbf{Ax} = \mathbf{d} + \varepsilon, \tag{1}$$

where $(\mathbf{d} + \varepsilon)$ is the vector of N travel time residuals and ε is the noise present in the data [*Nolet*, 1987]. Because we used a global data set, we were, in practice, forced to do the ray tracing in a spherically symmetric Earth model. Ray bending will possibly lead to a shift in the exact location of the anomalies, though the effect on integrated velocity anomalies is difficult to assess, especially when finite frequency effects, which tend to reduce the dependency of the travel time to the exact ray location [*Marquering et al.*, 1998; *Tong et al.*, 1998], are taken into account. Similarly, event mislocations will lead to errors. *Tarantola* [1987] argues that modeling errors are equivalent to data errors in an equation such as (1). The model vector $\mathbf{x}$ includes velocity updates as well as corrections for the hypocenter location and station statics. We note that *Bijwaard et al.* [1998] estimate the standard deviation in the EHB data to be as low as 0.3 s, in accordance with our finding that the corrections have a small effect on the tomographic solution but are helpful to stabilize the inversion.

We solve (1) with the iterative matrix solver LSQR. The inner workings of LSQR have been discussed extensively else-

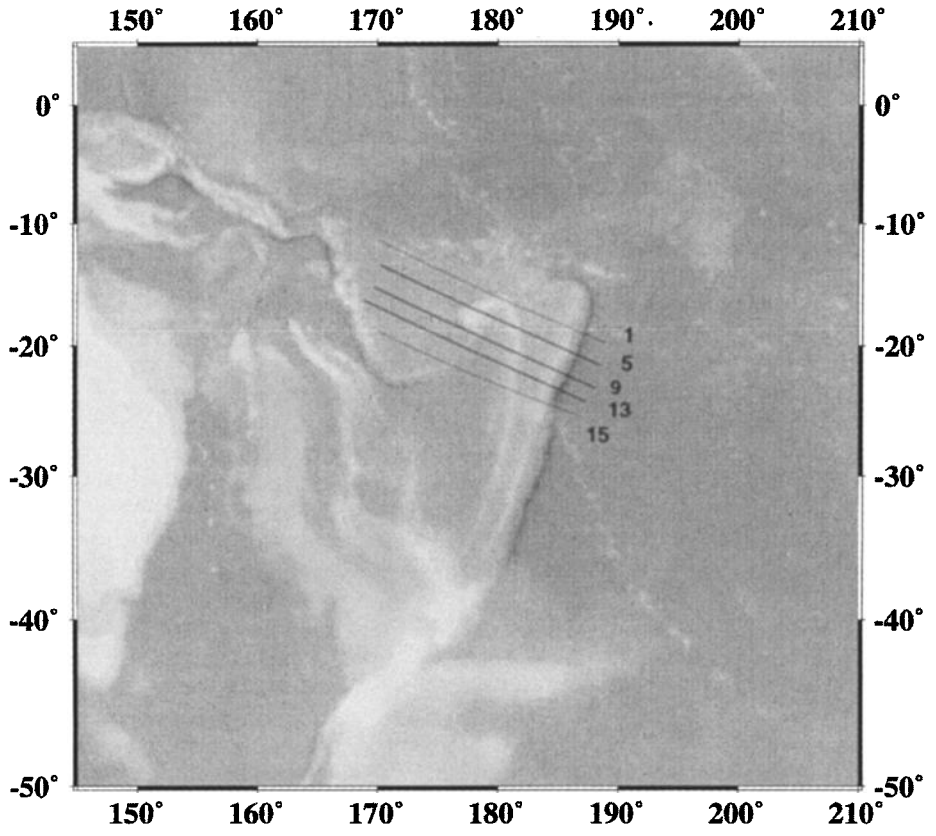

Figure 3. A map of the southwest Pacific region; the dark lines perpendicular to the trench denote the location of the slices depicted in Plates 1 and 2. The Tonga slab forms a hook north of 19°S at the location where the Vitiaz trench was once an active continuation of the Tonga trench to the northwest. Below 25°S is the Kermadec trench, which in the tomographic images has a less continuous slab. The ray coverage and resolution are reduced south of 25°S.

where [*Paige and Saunders*, 1982; *Nolet and Snieder*, 1990; *Deal and Nolet*, 1996a]. Here it suffices to say that LSQR converges to the minimum-norm, least squares solution by adding orthogonal vector components to the approximate solution at each iteration. In our case, convergence requires between 50 and 100 iterations.

Because the data vector includes noise, the converged solution to (1) may contain extreme fluctuations over short distances. These are known to be artifacts caused by the inversion trying to accommodate the noise through excessive variations in the model. In order to reduce this effect we not only damp the solution (see below) but also require the model to have a certain degree of smoothness. Intuitively, one should expect the velocity at a given node to be related to the neighboring nodes. This constraint is implemented by using a linear smoothing matrix **S** [*Spakman and Nolet*, 1988] to define a smooth solution vector $\mathbf{x}_{\text{smooth}}$,

$$\mathbf{Sy} = \mathbf{x}_{\text{smooth}}. \tag{2}$$

In our case the smoothing is a typical Gaussian function which extends over roughly three nodes in each direction. The elements in each row of **S** sum to 1.0, and the matrix is almost full rank, indicating the product **AS** has almost the same rank as **A**. Therefore model resolution is not significantly affected by the smoothing, but whenever the lack of resolving power allows, the smoothing matrix partially redistributes the slowness deviation at each node to the nearest neighboring nodes. Putting (2) into (1) gives [*Spakman and Nolet*, 1988]

$$\begin{aligned} \mathbf{ASy} &= \mathbf{d} + \varepsilon, \\ \mathbf{A'y} &= \mathbf{d} + \varepsilon, \\ \mathbf{x}_{\text{smooth}} &= \mathbf{Sy}. \end{aligned} \tag{3}$$

With the inclusion of a smoothing matrix we find a modified minimum-norm solution. However, smoothing alone is not enough to guarantee that noise in the data will not lead to numerous artifacts in the final solution. We must also damp the solution.

Damping creates a trade-off between fitting the noisy data and minimizing the changes between the model and a given reference model [*Menke*, 1989]. Once the model norm grows too large, the solution often contains unrealistic structures or artifacts which are caused primarily by noise or errors in the data. In our case we need a precise method for choosing the final solution. Since our intention is to fit a theoretical model for slab temperatures to the velocity perturbations in **x**, the goal is to find the tomographic model with velocity perturbations approaching those in the "true" Earth, while minimizing the artifacts caused by an overzealous inversion trying to fit the noise in the data. This requires us to know the statistics of the noise. Fortunately, independent estimates for the variance of the noise exist for ISC data.

The degree of damping introduced into the inversion is based on the expected value of the misfit, χ^2, which is derived from the variance of the noise and the number of data. The statistical estimates for the noise are summarized in Table 1. We take estimates for the variance of the incoherent portion of the signal for ISC *P* waves from *Gudmundsson et al.* [1990]. This will probably overestimate the noise level in the EHB data used in this study. Estimates for core phases come from *Rogers and Wahr* [1993], who performed a statistical analysis on *PKP* and *PcP* phases after relocating and reidentifying the arrivals employing the same method used on our data [*van der Hilst and Engdahl*, 1992; *Engdahl et al.*, 1998].

Multiplying both sides of (1) with the inverse square root of the data covariance matrix $\mathbf{C}_d^{-1/2}$ causes the inversion to appropriately weigh each datum based on its estimated uncertainty. After multiplying (1) by $\mathbf{C}_d^{-1/2}$, which we assume is diagonal,

$$\mathbf{C}_d^{-1/2}\mathbf{A}\mathbf{x} = \mathbf{C}_d^{-1/2}(\mathbf{d} + \varepsilon), \tag{4}$$

the right-hand side is dimensionless and the incoherent component of the data has a variance of one.

The dimensionless version of (1) can be posed as

$$\hat{\mathbf{A}}\hat{\mathbf{x}} = \hat{\mathbf{d}} + \hat{\varepsilon}, \tag{5}$$

where $\hat{\varepsilon}$ follows a normal distribution $N(0, 1)$. Then the misfit is

$$\chi^2 = \|\hat{\mathbf{A}}\hat{\mathbf{x}} - \hat{\mathbf{d}} - \hat{\varepsilon}\|^2, \tag{6}$$

for the case where each datum has been scaled to have unit variance. For the true Earth solution $\mathbf{x}_{\text{true}}$ we know

$$E\{\chi^2_{\text{true}}\} = \|\hat{\varepsilon}\|^2 \approx N. \tag{7}$$

The inverse problem is damped such that the LSQR solution converges to a solution with $\chi^2 = N$. Figure 4 is a plot of the χ^2 misfit versus LSQR iterations. The region of acceptable models in the M-dimensional model space will have a misfit which obeys a chi-square distribution with N degrees of freedom [*Parker*, 1994]. Asymptotically, for large N the chi-square distribution approaches a normal distribution with mean N and $\sigma_x = \sqrt{2N}$. Our simple statistical reasoning is entirely based on the overly optimistic notion that seismic data obey Gaussian statistics. It has been shown previously [*Jeffreys*, 1936; *Buland*, 1984] that this is not entirely true; therefore, since we are ignoring the tails present in the distribution of the seismic data, we choose to define a region of acceptable misfits based on the $6\sigma_x$ level (as opposed to the more standard $2\sigma_x$ or $3\sigma_x$ levels). Using $6\sigma_x$ still provides a very small region of acceptable misfit values. The acceptable region for χ^2 misfits is shown in Figure 4; all the minimum-norm solutions that we inspected within $E\{\chi^2\} \pm 6\sigma_x$ appear to be nearly identical.

Table 1. Statistical Estimation of the Variance in the ISC Delay Time Data Used in This Study

Major Ray Types	Variance for Incoherent Part of Signal (σ^2), s^2
P ($0° \le \Delta \le 30°$)	0.75–1.30
P ($30° \le \Delta \le 90°$)	0.31–0.63
P ($90° \le \Delta \le 100°$)	0.45–0.85
PcP	2.85
*PKP*ab	1.70
*PKP*bc	1.40
*PKP*df	2.92

Data from *Gudmundsson et al.* [1990] and *Rogers and Wahr* [1993].

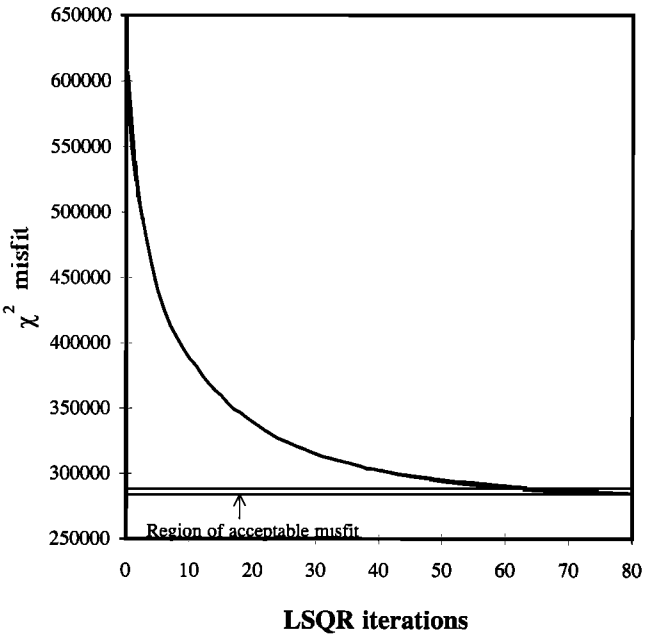

Figure 4. The change in χ^2 misfit as a function of the number of LSQR iterations. The horizontal lines denote the region of acceptable solutions based on the expected value of the misfit; solutions within the acceptable region show almost no discernible differences. The width of the acceptable region corresponds to a deviation of a few percent in the estimates of the variance in the data.

Since we know the true solution lies within a given region around the least squares solution, our goal is to lessen the distance between the best fit model and the true solution by incorporating additional information. In this study the additional information includes the notion that slab velocity variations are strongly influenced by temperature and that the temperature distribution satisfies physical laws. Neither are very certain, but we can bias our model toward such a theoretical solution and only deviate from it for as far as the data allow us to do so.

3. Inverting for Slab Thickness and Mantle Temperature

3.1. Theoretical Temperature Model

The result of the tomographic inversion is a three-dimensional model of seismic velocity deviations from the ak135 background model. The high-velocity slab is the feature of the tomogram we want to enhance using a theoretical temperature model. To first order, we relate the positive velocity anomalies in the slab to temperature deviations from the ambient mantle temperature. To translate theoretically predicted temperature anomalies to velocity perturbations, we use the thermal coefficient of seismic velocity, dV/dT. We assume the derivative is constant over the pressure range involved. Using laboratory data from *Duffy and Anderson* [1989] and assuming a slab petrology similar to that proposed by *Ringwood* [1982], we calculate the value of dV/dT to be 4.8×10^{-4} km s^{-1} C^{-1}. This value is also consistent with the measurements based on residual sphere analysis by *Creager and Jordan* [1986] and

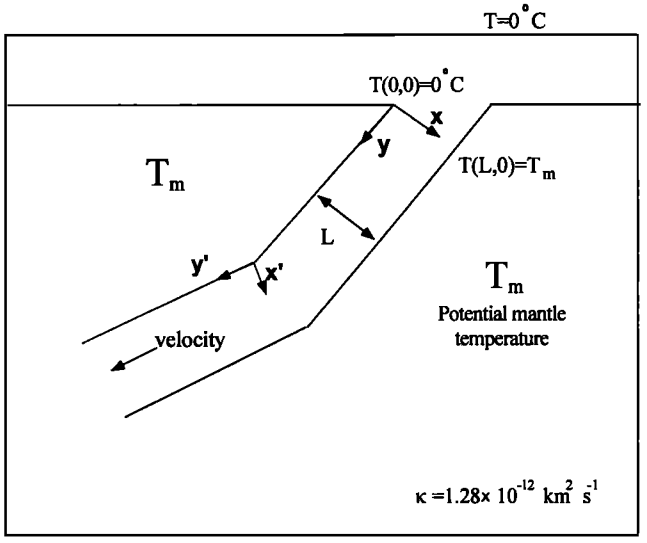

Figure 5. A schematic illustration of a subducting slab including a change in dip angle. The model parameters are labeled.

Fischer et al. [1991]. Since our travel times are representative of impulsive P waves with frequencies of the order of 1 Hz, we believe this value accurately reflects the anharmonic effect of temperature on the seismic waves in our data set. The laboratory determined value of dV/dT that accounts for the anharmonic effects of temperature will be less appropriate for lower-frequency arrivals because of attenuation-related velocity dispersion effects [*Goetze*, 1977; *Karato*, 1993].

To more efficiently compare the tomographic result to a synthetic slab model based on a theoretical temperature model, we choose to use an analytical expression in place of a finite difference algorithm to predict slab temperatures. The temperature model used is a slightly modified version of the solution given by *Davies and Stevenson* [1992, appendix]:

$$T = T_m + (T_m - T_0)\left\{\frac{(x-l)}{2l}[\mathrm{erf}(b) - \mathrm{erf}(a)] - \alpha\left[\frac{e^{-b^2} - e^{-a^2}}{l\sqrt{\pi}}\right]\right\}, \quad (8)$$

where $a = -x/\alpha$, $b = -(x - l)/\alpha$ and $\alpha = \sqrt{4\kappa y/v_y}$. T_m is the potential mantle temperature, T_0 is the temperature at the top of the slab at the point when the slab enters the asthenosphere, l is the slab thickness, v_y is the downgoing subduction velocity in the direction of the slab motion, and κ is the heat diffusivity. The coordinate system is such that y is positive down the dip direction of the slab and x is positive down into the mantle beneath the slab (Figure 5). While this may be a simplified model, one of the issues we hope to address is how well a simple model can explain the tomographic observations.

We checked the accuracy of (8) by comparing it to the outcome of the finite difference algorithm created by N. H. Sleep [*Toksoz et al.*, 1973]. The differences between the analytical equation in (8) and the finite difference code are insignificant for our purposes; the largest discrepancy is over a narrow region in the center of the slab and is ~100°C. Figure 6 shows the thermal slab profile calculated using the analytical model (equation (8)). The evolution of the temperature profiles across the slab with increasing depth is shown in Figure 7. All calculations are done using potential temperatures [*McKenzie*, 1970].

3.2. Two-Dimensional Slices

Using a constant value for dV/dT, we are able to employ (8) to convert temperature variations to velocity anomalies

$$\Delta V = [T(\mathbf{x}) - T_m]\frac{dV}{dT}, \quad (9)$$

where $T(\mathbf{x})$ is the temperature predicted by the theoretical temperature model and the vector $\mathbf{x}$ contains the parameters in the analytical temperature model. The temperature profile for a two-dimensional slab cross section is converted to velocity perturbations using (9) and then compared to perpendicular cross sections through the tomographic slab model. Instead of comparing the velocity perturbations at individual nodes in the model, we compare the integrated value of the velocity deviations for two depth regions. The integral over all positive velocity anomalies in the slab region between 100 and 350 km depth is calculated for both the tomogram as well as the predicted slab model. The integral is also calculated between 450 and 660 km. The misfit is expressed as

$$F_i = \int_{V_i} [v_{\mathrm{mod}}(\mathbf{r}) - v_{\mathrm{tomo}}(\mathbf{r})]\, d^2\mathbf{r}, \quad (10)$$

where $\mathbf{V}_i$ is the volume defined by all positive anomalies excluding 350–450 km depth for slice i, and v_{mod} and v_{tomo} are the velocity deviations at location $\mathbf{r}$ for the theoretical model and tomogram, respectively. A nonlinear conjugate gradient optimization based on the *Fletcher and Reeves* [1964] algorithm is used to minimize the objective function (equation (10)). The parameters we invert for are slab thickness and potential mantle temperature while keeping slab velocity and the heat diffusivity constant. The integral over all positive velocity anomalies is not dependent on the values used for slab velocity and diffusivity since the physical model used is for the steady state thermal regime. The velocity and diffusivity affect the shape of the temperature profile but not the integrated value of velocity

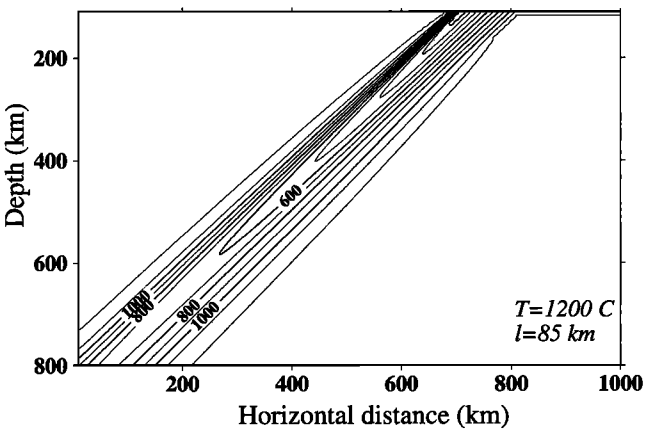

Figure 6. Two-dimensional temperature profile based on the analytical model shown in equation (8). The input parameters are mantle potential temperature T_m = 1200°C, slab thickness l = 85 km, plate velocity of 7.5 cm yr^{-1}, heat diffusivity of 1.28 × 10^{-12} km^2 s^{-1}, and angle of subduction of 45°.

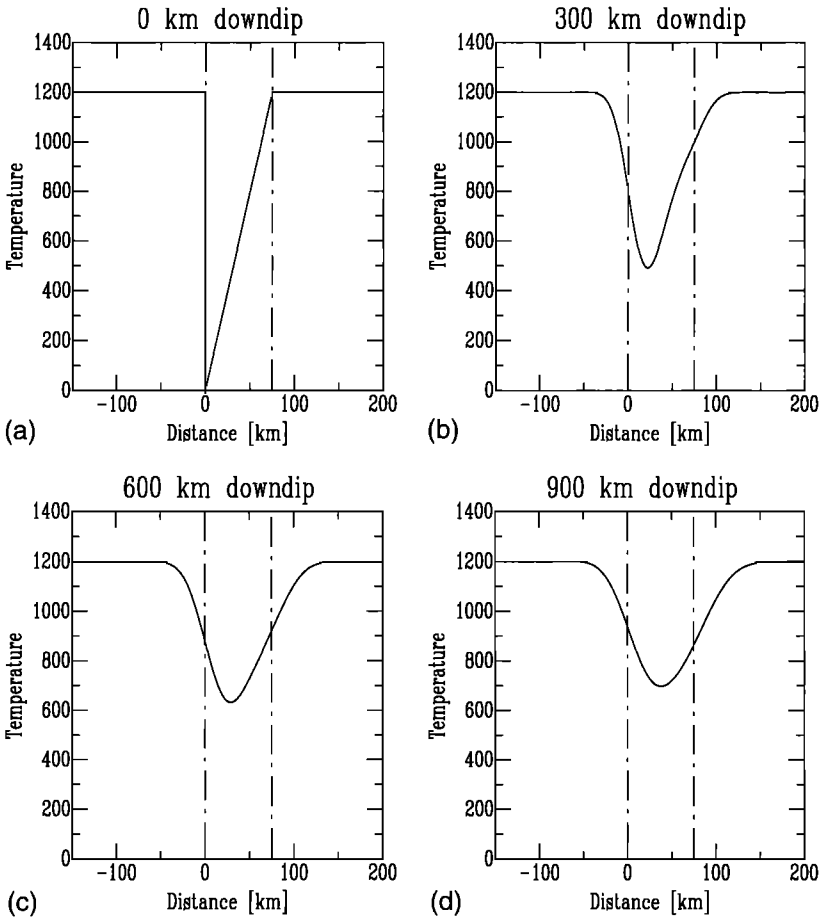

Figure 7. The temperatures across the slab at a given distance down the length of the slab. (a) At the top of the slab (the point where the slab enters the asthenosphere and the flow turns parallel to the slab, 100 km), showing the initial condition; (b–d) obtained by solving heat flow equation (8) using the same parameters as in Figure 6. The dashed lines indicate the initial position of the slab.

(or temperature) deviations. We use a value of $v = 7.5$ cm y^{-1} [*Jarrard*, 1986] and $\kappa = 1.28 \times 10^{-12}$ km^2 s^{-1}. The position of the slab and angle of subduction is constrained by the initial tomographic images as well as slab seismicity. The position of the slab in our images is very similar to the extremely high resolution images of *Zhao et al.* [1997], who used a data set enhanced by local ocean bottom seismometer data.

The depth regions over which we compare the tomogram to the predicted model are chosen so the olivine to spinel phase change will not affect our results. Phase changes are purposely absent in the simplified analytical model because of the uncertainty involved in trying to map the thermal effects of phase changes onto the slab. If the phase change from olivine to spinel occurs at the same depth in the slab and in the ambient mantle, then the results of the analytical model would be correct across the phase change. However, the analytical model will be incorrect if the depth of the phase change associated with the 400-km discontinuity is elevated within the slab due to its lower temperature, or lowered if metastable olivine persists within the slab. To avoid the problems associated with the olivine to spinel discontinuity, the region over which the phase change is thought to occur (350–450 km) is disregarded when we compare the theoretical temperature model to the tomogram; therefore the depth of the phase change within the slab does not affect our final results. This implies we are confident that material above 350 km is still in an olivine structure, both within the slab as well as the surrounding mantle. Likewise, below 450 km we assume the transformation to the denser spinel phase is complete.

The smoothing of the tomogram in the inversion step has a negligible effect on the results since we integrate over positive velocity deviations in the slab region when comparing the misfit between the tomogram and the predicted slab model. Our method is based on the total overall effect of a cool slab on velocity and not on local, high-resolution effects. The use of integrated anomalies causes a loss of resolution in the modeling, and as we show in section 5, we are not able to separate the effect of slab thickness from that of the ambient mantle temperature, but it offers various advantages that we briefly discuss here. *Koper et al.* [1998] show the inability of even a very dense data set to resolve details of the velocity structure in the slab. *Tong et al.* [1998] show that finite frequency effects may reduce the travel time anomaly, while at the same time spread it over a wider area such as to preserve the integrated value of the delay over a larger volume. The integrated value is an average and as such more precisely determined than local values.

When choosing which cross sections through the tomographic model to compare to the theoretical slab model, we are careful to use only those slices which we feel are representative of the three-dimensional velocity model. Slices not represen-

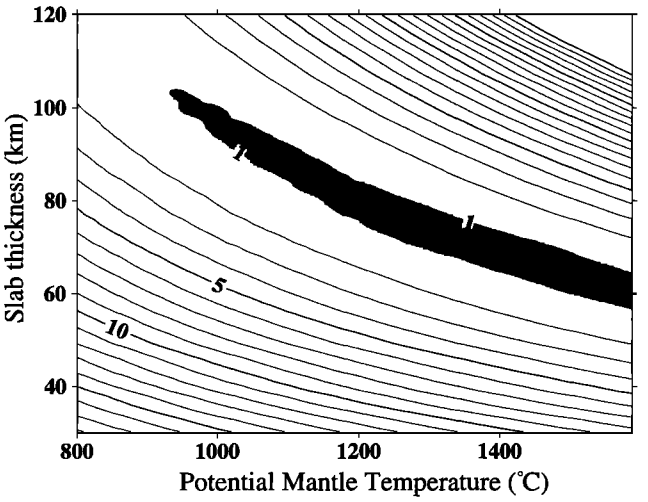

Figure 8. The trade-off curve for the nonlinear optimization between mantle temperature and slab thickness. Based on the results from the tomographic imaging, the acceptable slab thickness and mantle temperature values are shown by the shaded region. Since the amplitudes of the velocity deviations in the damped, least-squares solution are assumed to be less than or equal to the deviations in the "true" Earth, we use figure 10 as an indication of the lower bounds on the mantle temperature and slab thickness parameters. The upper bound for the temperature and thickness parameters is shown in figure 11. The contour interval is 1 and the misfit values have been scaled such that an acceptable misfit is less than 1.

tative of a continuous subducting regime are not used in the nonlinear optimization for temperature parameters; however, they are included in the final three-dimensional synthetic slab. For example, slice 13 (Plate 2) depicts a slab which has been strongly deformed between 400 km and 550 km and is less likely to be representative of a steady state process.

3.3. Three-Dimensional Inversion

The nonlinear optimization is performed independently on each of the well-resolved, typical two-dimensional cross sections. The optimal values for the parameters in the slab temperature model vary somewhat with different cross sections. Some variation among the parameters is warranted, such as dip angle and position of subduction. Other parameters such as mantle temperature and slab thickness should be fairly consistent over a number of nearby slices. However, certain trade-offs exist between the slab thickness and mantle temperature which result in nearly equivalent fits to the tomogram for different values for the parameters. To reconcile the variations among the parameters for the different cross sections, we look for regions in the model space where the trade-off curves for different cross sections intersect. Each independent cross section may have a family of solutions that satisfy the misfit, and for the final solution we choose one that optimally satisfies all of the cross-sectional slices.

The optimal solutions from each of the different cross sections are combined analytically using Newton's method. If $F_i(\mathbf{u}_0)$ is the objective function for the ith cross-sectional slice at $\mathbf{u}_0$, where vector $\mathbf{u}$ is the solution vector which contains the parameters to the objective function, then the Taylor series approximation for the objective function is

$$F_i(\mathbf{u}) = F_i(\mathbf{u}_0) + \mathbf{g}_i(\mathbf{u}_0)^T(\mathbf{u} - \mathbf{u}_0) + \tfrac{1}{2}(\mathbf{u} - \mathbf{u}_0)^T\mathbf{H}_i(\mathbf{u}_0)(\mathbf{u} - \mathbf{u}_0), \quad (11)$$

where $\mathbf{g}_i(\mathbf{u}_0)$ is the gradient for the ith section and $\mathbf{H}_i(\mathbf{u}_0)$ is the symmetric Hessian matrix of the objective function for the ith section and is calculated using finite differences. In order to find an optimal solution for all of the cross sections we define a new objective function which is a sum of the individual objective functions for each slice,

$$J(\mathbf{u}) = \sum_{i=1}^{n} F_i(\mathbf{u}), \quad (12)$$

where n is the number of cross sections. A necessary condition for the minimization of the new objective function J is that $\nabla J(\mathbf{u}) = 0$. This gives

$$\mathbf{H}'\mathbf{u} = \sum_{i=1}^{n} [\mathbf{H}_i(\mathbf{u}_i)\mathbf{u}_i - \hat{\mathbf{g}}_i(\mathbf{u}_i)], \quad (13)$$

where

$$\mathbf{H}' = \sum_{i=1}^{n} \mathbf{H}_i(\mathbf{u}_0^i). \quad (14)$$

For those variables that we wish to hold constant in each individual slice, such as dip angle and position of the slab, we set the elements in the corresponding rows and columns of the Hessian to zero. The position of the slab and dip of the slab are determined based on the tomographic results as well as the location of seismicity. The inverse of $\mathbf{H}'$ is calculated using singular value decomposition and can be stabilized by disregarding any eigenvalues which fall below a given threshold.

Inspection of $J(\mathbf{u})$ as a function of T_m and l shows that we are unable to uniquely specify the mantle temperature and slab thickness. Instead, we find a small region of acceptable temperature and thickness combinations. The misfit contour plot showing the optimal values for T_m and l, based on all of the slices used in the nonlinear optimization, is shown in Figure 8; the shaded region indicates the area of acceptable solutions. In order to obtain the most appropriate value for the thickness of the lithosphere we need a constraint for the temperature of the mantle.

The phase transition from γ-spinel to perovskite can be used to specify the temperature at 660 km. The temperature of the phase transition to the perovskite structure is not substantially affected by the Mg to Si ratio or the percent Fe in olivine in the mantle [*Ito and Takahashi*, 1989] and therefore is an ideal choice for fixing the temperature at 660 km. Laboratory data on the spinel to perovskite phase change indicate a temperature of 1675°C at 660 km [*Boehler and Chopelas*, 1991, 1992]. Extrapolating this temperature to the surface (P = 0), assuming an adiabatic gradient, gives $T_m \approx 1180° \pm 100°$C (F. Stacey, personal communication, 1996). Using this value for the potential mantle temperature gives an optimal slab thickness of 80 km in the Tonga region. However, this value represents the lower bound on l since the contour plot for misfit as a function of T_m and l is based on the initial, damped, least squares tomogram.

4. Null-Space Shuttle

In order to create a theoretical three-dimensional model of velocity deviations we need a mechanism to combine two-

dimensional slab cross sections into a three-dimensional model. The optimal temperature parameters are used to predict the slab structure for all slices, even those slices not included in the nonlinear inversion. For those slices which are deformed and have kinks in the slab structure we use an approximation in the coordinate system shown in Figure 4. We do not feel the approximation made by bending the coordinate system in order to facilitate a kink in the temperature models is major. As shown later in this section, the null-space shuttle will correct us when and where the approximation is wrong. Finely spaced two-dimensional cross sections are then combined and interpolated to form a three-dimensional model.

Using the final parameters to the theoretical temperature model, we are able to create a theoretical tomogram based on the temperature model. The theoretical slab images (see Plate 1) do not contain any structure other than the subducting slab since the simple temperature model only specifies temperatures within the descending slab. Areas far away from the slab are left unchanged from the initial tomographic model. The new velocity model which includes the theoretical slab based on the temperature model no longer satisfies the original seismic data. In order to reconcile the misfit to the EHB delay times caused by the theoretical slab, we utilize the null-space shuttle [*Deal and Nolet*, 1996b]. The difference between the original tomogram, which satisfies the delay time data, and the theoretical slab, which does not satisfy the delay times, is projected onto the null-space from the tomographic inversion. If the difference between the two models can be projected onto the null-space of matrix **A** (equation (1)), then the theoretical model is consistent with the travel time data. If

$$\Delta \mathbf{x} = \mathbf{x}_{\text{theoretical}} - \mathbf{x}_{\text{tomogram}} \tag{15}$$

is the difference between the two models, where $\mathbf{x}_{\text{tomogram}}$ is a solution to (1), then using the null-space shuttle operator, **NS**, we can find the component of $\Delta \mathbf{x}$ that lies in the null-space [*Deal and Nolet*, 1996b]:

$$\mathbf{NS}(\Delta \mathbf{x}) = \Delta \mathbf{x}_{\text{null-space}}, \tag{16}$$

and define our final image as

$$\mathbf{x}_{\text{final}} = \mathbf{x}_{\text{tomogram}} + \Delta \mathbf{x}_{\text{null-space}}. \tag{17}$$

By definition

$$\mathbf{A}\Delta \mathbf{x}_{\text{null-space}} = 0, \tag{18}$$

and therefore

$$\mathbf{A}(\mathbf{x}_{\text{final}}) = \mathbf{d}_{\text{EHB}}. \tag{19}$$

We require that the misfit of our improved image ($\mathbf{x}_{\text{final}}$) falls within the region of acceptable misfits as defined previously. The misfit of the initial, least squares solution and the misfit of the final model are comparable. The initial tomogram is a minimum-norm solution, while the final model contains null-space components introduced by the theoretical temperature model.

5. Results

5.1. Slab Morphology

The results of the tomographic inversion are shown in Plates 1 and 2. Slices are taken every 0.5° along the trench with slice 1 to the north; only a subset of the slices is shown. The slices depicted in Plates 1 and 2 are marked on the map in Figure 3. Many of the features seen in our tomographic results are similar to those described by *van der Hilst* [1995]. The major differences reflect the improved resolution we obtain by using 50-km-spaced nodes as opposed to larger cells to parameterize the velocity model. The more recent study by *Zhao et al.* [1997] uses cells 25 km high and 50 km wide to achieve a very high resolution result which has similar characteristics to our model. At depths below 400 km the tomographic images of the Kermadec slab show a less continuous slab that appears to break into pieces between 29°S and 40°S. Since the images obtained for this region show a discontinuous slab, we choose not to optimize the temperature model against the images of the Kermadec slab. One possible reason for the Kermadec slab to appear broken in the tomographic images is the decreased ray coverage in the area.

Below 600 km depth in slices 9–12 there is a large amount of high-velocity material beneath the South Fiji Basin. This material has probably been subducted 10–20 m.y. ago at the Tonga Trench or the Vitiaz Trench [*Hamburger and Isacks*, 1987]. The interaction of the lithospheric material from previous subduction zones may be responsible for the slab deformation seen in the central part of the Tonga slab between 400 and 500 km.

The slab images in slices 1–4 show the slab's dip decreasing at ~400 km depth. The slab appears to become horizontal below 500 km in slices 1 and 2 (farthest north), while later slices show the slab possibly continuing through 660 km. Cross sections in the vicinity of 24°S (slices 10–13, Plate 1) show the dip of the slab increasing dramatically around 400 km depth; below 500 km the dip of the slab appears to return to normal. This feature has been noted previously by *Giardini and Woodhouse* [1984], who examined earthquake locations in the Benioff zone. One possible cause for the deformation is the interaction of the slab with remnants of previous subduction zones, however, the tomographic models do not image any high-velocity features nearby the slab in this region. Another possible explanation given by *Giardini and Woodhouse* [1986] is that the slab deformation is a result of flow in the mantle. Because of the unusual deformation inferred from slices 10–13, we do not include them in the nonlinear inversion for temperature parameters.

Central slices (e.g., slices 5 and 9) show the slab with a fairly constant dip; these slices also show a horizontal layer of high-velocity material above 660 km as well as a substantial amount of high-velocity material below 660 km. The high velocities at depth occur horizontally over distances of 700–1100 km. Even though most of the tomographic images remain ambiguous about the fate of the subducted material when it reaches 660 km depth, our work demonstrates that the high velocities west of the Tonga slab, both above and below 660 km, are required by the data. This observation is discussed further in section 5.3 on the back projection method. However, it is apparent that the slab encounters some type of resistance at 660 km. Our images are most consistent with models that explain partial slab penetration into the lower mantle [*van Keken et al.*, 1996], or intermittent penetration.

5.2. Slab Thickness and Resolution

During the inversion for slab thickness we assume that the tomographic velocity deviations in the slab region are slightly less than those in the true Earth due to damping. Therefore the slab thickness estimate obtained should be viewed as lower bounds for the true Earth value. Since the initial tomogram

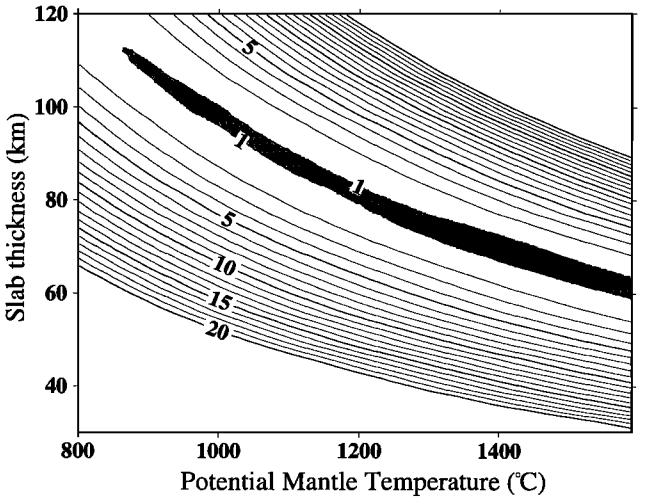

Figure 9. The contour plot of the misfit function using the filtered tomographic model which has the highest slab velocity deviations that are permitted by the data. The shaded region depicts the area of acceptable T_m and l combinations for the upper bounds. Figure 8 shows the lower bounds for potential mantle temperature and slab thickness, while Figure 9 shows the upper bounds.

serves as the lower end-member for velocity deviations (and hence T_m and l), we use the null-space to find a model to serve as the upper end-member. To do this, we modify the initial tomogram by replacing the slab region with a theoretical slab based on unrealistically large values for mantle temperature and lithosphere thickness. Of course, the model with the unrealistically thick slab does not satisfy the seismic data. We then use the null-space projection operator to find the velocity model with the maximum slab velocity anomaly still allowed by the data. Using this end-member model to perform the nonlinear optimization for the temperature parameters results in the T_m versus l contour plot shown in Figure 9. The shaded area shows the region of optimal T_m and l combinations based on the upper end-member velocity model. In this case, if we again assume $T_m \approx 1180°C$, we find a slab thickness of 84 km. Thus, within the resolution of the tomographic inversion we are able to constrain the slab thickness to lie between 80 and 84 km. To do this, we must add the uncertainty due to the uncertainty in T_m (7.7 km for 100°C). The resulting uncertainty in l is therefore estimated to be $\sqrt{7.7^2 + 2^2} = 8$ km. However, the uncertainty in T_m mainly acts as a "baseline" shift. If T_m is constant along the slab, we expect to resolve changes in thickness exceeding the uncertainty of 4 km. In our analysis we have used commonly used values for various physical parameters. While our solution is rather insensitive to most of them, a change in the value of $dV/dT = 4.8 \times 10^{-4}$ km s^{-1} °C^{-1} (averaged over all depth levels) would lead to a bias in our temperature estimates for the slab and, consequently, a bias in the thickness. Similarly, if the mantle is substantially higher in temperature, as recently suggested by *Hofmeister* [1999], a bias in the thickness will result which can be inferred (for a particular T_m from Plate 2 and Figure 8). Our error estimate of 8 km does not include such systematic errors, it is primarily meant to give an indication whether changes in slab thickness are resolved or not.

Our final result for the optimal T_m and l is based on the lower and upper bounds discussed above. Each time we use the null-space projection to eliminate those parts of a filtered model which are not in the null-space, we require the final misfit to be within the level specified in Figure 4. Using a value of $T_m \approx 1180°C$, our results suggest a slab thickness of 82 ± 8 km.

5.3. Enhanced Images After the Null-Space Shuttle

Besides using the seismic data to constrain the physical parameters (T_m and l) in the theoretical temperature model, we want to use the temperature model to enhance the tomogram. Two cross sections through the theoretical slab velocity image based on our final choice of temperature parameters are shown in Plate 1. The initial position of the slab and the dip are determined independently for each slice based on the initial tomogram. Since the simple thermal model only specifies temperatures, which are converted to seismic velocities using the parameter dV/dT, there is no structure away from the slab or below 660 km. The three-dimensional velocity model based on our temperature model (equation (8)) has a χ^2 misfit of 4.53×10^5, compared to a misfit of 3.60×10^5 for the LSQR solutions. Clearly, the synthetic slab model does not satisfy the EHB data.

In order to constrain the theoretical slab velocity model to fit the original travel time data, the portion of the theoretical slab image which is not consistent with the seismic data is removed from the model using the null-space projection. The resulting images after the projection are shown in Plates 1 and 2. The new corrected velocity model has a χ^2 misfit of 3.66×10^5 which is within the region of acceptable misfits shown in Figure 4. The new tomograms shown in Plates 1 and 2 are from the velocity model which most closely resembles the theoretically derived slab model while still satisfying the seismic data.

Previously, we mentioned that the high-velocity material below 660 km, as well as that laid down on top of the 660-km discontinuity, is required by the data. This is seen in Plates 1 and 2; the theoretical slab model has no high velocities to the west of where the slab initially reaches 660 km. However, after projecting the difference between the theoretical model and the tomogram onto the null-space, we see high velocities above and below 660 km in the final model. We conclude that these high velocities are required by the data.

Another important result concerns the low-velocity zones surrounding the subducting lithosphere. The theoretical velocity model has no low-velocity zones surrounding the slab; however, after projecting onto the null-space, the low-velocity anomalies return in the final solution but to a lesser extent. This means that the low-velocity zones are required by the seismic data in order to achieve the desired misfit, but the amplitude of the low velocities in the initial tomographic solution are higher than necessary. The causes for the low-velocity zones at depth are debatable, and they are often thought to be artifacts of the linearized inversion. One speculative explanation for the low-velocity zones has been partial melt caused by the release of volatiles, primarily H_2O and CO_2, into the mantle. However, the release of H_2O and CO_2 into the mantle is usually expected to occur above 120 km depth, and in order for volatiles to reach greater depths we need to invoke superhydrous phases [*Thompson*, 1992; *Nolet and Zielhuis*, 1994]. Other possible causes for the low velocities include flow-induced anisotropy in the mantle immediately adjacent to the slab. *Christensen and Salisbury* [1979] have established that the *a* axis (fast direction) for olivine will orient in the direction of the flow line. If a large fraction of rays sampling the region

beneath the slab travels nearly perpendicular to the flow direction, then there is a possibility that a low-velocity signal may be partially realized due to preferred lattice orientations in the olivine crystals. Though if this were the case, the region of low velocities should exist only in regions of large shear strain, i.e., probably within 60–120 km of the slab. Most of the images show broader regions of low velocities extending several hundred kilometers away from the slab. At some places in this region the low velocities can be traced down to the core-mantle boundary (CMB) and are possibly related to upwelling beneath the Society Islands. The purpose of this paper is not to unequivocally explain these low-velocity regions, but our results do indicate that the low-velocity zones are required by the data in order to satisfy the linearized inversion problem as currently posed.

6. Conclusions

We have presented a method which allows us to substantially enhance tomographic images without corrupting the data fit. In the process we are able to provide evidence supporting a theoretical slab temperature model and to obtain a range of acceptable values for mantle temperature and slab thickness for the Tonga slab. Assuming a potential mantle temperature of 1180°C ± 100°C, we determine a slab thickness of 82 ± 8 km for a region of the Tonga slab. We have also shown that the gap in the slab near 325 km depth seen in previous tomographic studies is not required by the data: our final images depict a much more continuous and narrow slab between 100 and 660 km.

A portion of the 1–3% low-velocity regions seen on both sides of the slab (especially beneath the slab) is required by the data. We can not eliminate these low-velocity zones by using only components in the null-space. The fate of the slab once it reaches 660 km is still debatable. In the Tonga region many of our slices indicate that the slab flattens at 660 km, and this high-velocity material is required in order to satisfy the data. There are regions, however, where we find substantial amounts of high-velocity material below 660 km, which implies some degree of slab penetration [see also *van der Hilst*, 1995].

Our method differs from earlier methods that use a priori information in that we use the tomogram to resemble a physical model after determination of the optimal model parameters. For example, *Tarantola* [1987] and *Abers and Roecker* [1991] impose a priori spatial correlations on the tomographic solution that are not tied to a physical model. *Lerner-Lam and Jordan* [1987] test for the minimum lithospheric thickness beneath continents consistent with seismic data but use no other constraints. In this paper we have shown how the null-space shuttle can be used to bias tomographic solutions toward optimized physical models, thus providing a convenient formalism for the testing of hypotheses, even those involving complicated modeling.

Acknowledgments. M.D. acknowledges support from NSF grant EAR-9526372 and from a Princeton University Honorific Fellowship. Seth Stein kindly gave us his version of the finite difference program to compute temperatures. We also thank Geoffrey Abers, Doug Wiens, and Domenico Giardini for their constructive and beneficial comments.

References

Abers, G. A., and S. W. Roecker, Deep structure of an arc-continent collision: Earthquake relocation and inversion for upper mantle *P* and *S* wave velocities beneath Papua New Guinea, *J. Geophys. Res.*, *96*, 6379–6401, 1991.

Bijwaard, H., W. Spakman, and E. R. Engdahl, Closing the gap between regional and global travel time tomography, *J. Geophys. Res.*, *103*, 30,055–30,078, 1998.

Boehler, R., and A. Chopelas, A new approach to laser heating in high pressure mineral physics, *Geophys. Res. Lett.*, *18*, 1147–1150, 1991.

Boehler, R., and A. Chopelas, Phase transitions in a 500 kbar–3000 K gas apparatus, in *High Pressure Research: Application to Earth and Planetary Sciences*, edited by Y. Syono and M. H. Manghnani, pp. 55–60, Terra Sci., Tokyo, 1992.

Buland, R., Residual statistics, *Terra Cognita*, *Ser. B*, *4*, 268, 1984.

Christensen, N. I., and M. H. Salisbury, Sesimic anisotropy in the oceanic upper mantle: Evidence from the Bay Islands ophiolite complex, *J. Geophys. Res.*, *84*, 4601–4610, 1979.

Creager, K. C., and T. H. Jordan, Slab penetration into the lower mantle beneath the Mariana and other island arcs of the northwest Pacific, *J. Geophys. Res.*, *91*, 3573–3589, 1986.

Davies, J. H., and D. J. Stevenson, Physical model of source region of subduction zone volcanics, *J. Geophys. Res.*, *97*, 2037–2070, 1992.

Deal, M. M., Tomographic image enhancement in slab regions: Tonga to Japan via the nullspace shuttle, Ph.D. thesis, 150 pp., Princeton Univ., Princeton, N. J., 1997.

Deal, M. M., and G. Nolet, Comment on "Estimation of resolution and covariance for large matrix inversions" by Zhang and McMechan, *Geophys. J. Int.*, *127*, 245–250, 1996a.

Deal, M. M., and G. Nolet, Nullspace shuttles, *Geophys. J. Int.*, *124*, 372–380, 1996b.

de Jonge, M. R., M. J. R. Wortel, and W. Spakman, Regional scale tectonic evolution and the seismic velocity structure of the lithosphere and upper mantle: The Mediterranean region, *J. Geophys. Res.*, *99*, 12,091–12,108, 1994.

Duffy, T. L., and D. L. Anderson, Seismic velocities in mantle minerals and the mineralogy of the upper mantle, *J. Geophys. Res.*, *94*, 1895–1912, 1989.

Engdahl, E. R., R. D. van der Hilst, and R. P. Buland, Global teleseismic earthquake relocation with improved travel times and procedures for depth determination, *Bull. Seismol. Soc. Am.*, *88*, 722–743, 1998.

Fischer, K. M., K. C. Creager, and T. H. Jordan, Mapping the Tonga slab, *J. Geophys. Res.*, *96*, 14,403–14,427, 1991.

Fletcher, R., and C. Reeves, Function minimization by conjugate gradients, *Comput. J.*, *7*, 149–154, 1964.

Gasparik, T., The role of volatiles in the transition zone, *J. Geophys. Res.*, *98*, 4287–4299, 1993.

Giardini, D., and J. H. Woodhouse, Deep seismicity and modes of deformation in Tonga subduction zone, *Nature*, *307*, 505–509, 1984.

Giardini, D., and J. H. Woodhouse, Deep seismicity and modes of deformation in Tonga subduction zone, *Nature*, *319*, 551–555, 1986.

Goetze, C. A., A brief summary of our present day understanding of the effect of volatiles and partial melt on the mechanical properties of the upper mantle, in *High Pressure Research*, edited by M. H. Manghnani and S. Akimoto, pp. 3–23, Academic, San Diego, Calif., 1977.

Gudmundsson, O., J. H. Davies, and R. W. Clayton, Stochastic analysis of global travel time data: Mantle heterogeneity and random errors in the ISC data, *Geophys. J. Int.*, *102*, 25–42, 1990.

Hamburger, M. W., and B. L. Isacks, Deep earthquakes in the Southwest Pacific: A tectonic interpretation, *J. Geophys. Res.*, *92*, 13,841–13,854, 1987.

Hirahara, K., A large-scale three-dimensional seismic structure under the Japanese Islands and the Sea of Japan, *J. Phys. Earth*, *25*, 393–417, 1977.

Hofmeister, A. M., Mantle values of thermal conductivity and the geotherm from phonon lifetimes, *Science*, *283*, 1699–1706, 1999.

Inoue, H., Y. Fukao, K. Tanabe, and Y. Ogata, Whole mantle *P*-wave travel time tomography, *Phys. Earth Planet. Inter.*, *159*, 294–328, 1990.

Ito, E., and E. Takahashi, Postspinel transformations in the system Mg_2SiO_4–Fe_2SiO_4 and some geophysical implications, *J. Geophys. Res.*, *94*, 10,637–10,646, 1989.

Jarrard, R. D., Relations among subduction parameters, *Rev. Geophys.*, *24*, 217–284, 1986.

Jeffreys, H., On travel times in seismology, *Bur. Seismol. Trav.*, *14*, 3–86, 1936. (Reprinted in *The Collected Papers of Sir Harold Jeffreys*,

vol. 2, *Observation Seismology*, pp. 36–120, Gordon and Breach, Newark, N. J., 1973.)

Jordan, T. H., Lithospheric slab penetration into the lower mantle beneath the Sea of Okhotsk, *J. Geophys.*, *43*, 473–496, 1977.

Karato, S., Importance of anelasticity in the interpretation of seismic tomography, *Geophys. Res. Lett.*, *20*, 1623–1626, 1993.

Kennett, B. L. N., E. R. Engdahl, and R. Buland, Constraints of seismic velocities in the Earth from travel times, *Geophys. J. Int.*, *122*, 108–124, 1995.

Koper, K. D., D. A. Wiens, L. M. Dorman, J. A. Hildebrand, and S. C. Webb, Modeling the Tonga slab: Can travel time data resolve a metastable olivine wedge?, *J. Geophys. Res.*, *103*, 30,079–30,100, 1998.

Lerner-Lam, A. L., and T. H. Jordan, How thick are the continents?, *J. Geophys. Res.*, *92*, 14,007–14,026, 1987.

Marquering, H., G. Nolet, and F. A. Dahlen, Three-dimensional waveform sensitivity kernels, *Geophys. J. Int.*, *132*, 521–534, 1998.

McKenzie, D. P., Temperature and potential temperature beneath island arcs, *Tectonophysics*, *10*, 357–366, 1970.

Menke, W., *Geophysical Data Analysis*, Academic, San Diego, Calif., 1989.

Nolet, G., Seismic wave propagation and seismic tomography, in *Seismic Tomography*, edited by G. Nolet, pp. 1–23, D. Reidel, Norwell, Mass., 1987.

Nolet, G., and R. Snieder, Solving large linear inverse problems by projection, *Geophys. J. Int.*, *103*, 565–568, 1990.

Nolet, G., and A. Zielhuis, Low *S* velocities under the Tornquist-Teisseyre: Evidence for water injection into the transition zone by subduction, *J. Geophys. Res.*, *99*, 15,813–15,820, 1994.

Oliver, J., and B. Isacks, Deep earthquake zones, anomalous structure in the upper mantle, and the lithosphere, *J. Geophys. Res.*, *72*, 4259–4275, 1967.

Paige, C., and M. Saunders, LSQR: An algorithm for sparse linear equations and sparse least squares, *Trans. Math. Software*, *8*, 43–71, 1982.

Parker, R. L., *Geophysical Inverse Theory*, Princeton Univ. Press, Princeton, N. J., 1994.

Ringwood, A., Phase transformations and differentiation in subducted lithosphere: Implications for mantle dynamics, basalt petrogenesis and crustal evolution, *J. Geol.*, *90*, 611–643, 1982.

Rogers, A., and J. Wahr, Inference of core-mantle boundary topography from ISC *PcP* and *PKP* traveltimes, *Geophys. J. Int.*, *115*, 991–1011, 1993.

Rubie, D. C., and C. R. Ross II, Kinetics of the olivine-spinel transformation in subducting lithosphere: Experimental constraints and implications for deep slab processes, *Phys. Earth Planet. Inter.*, *86*, 223–241, 1994.

Spakman, W., and G. Nolet, Imaging algorithms, accuracy and resolution in delay time tomography, in *Mathematical Geophysics*, edited by N. J. Vlarr, G. Nolet, M. J. R. Wortel, and S. A. P. L. Cloetingh, pp. 155–187, D. Reidel, Norwell, Mass., 1988.

Spakman, W., M. J. R. Wortel, and N. J. Vlaar, The Hellenic subduction zone: A tomographic image and its geodynamic implications, *Geophys. Res. Lett.*, *15*, 60–63, 1988.

Sykes, L. R., The seismicity and deep structure of island arcs, *J. Geophys. Res.*, *71*, 2981–3006, 1966.

Tarantola, A., *Inverse Problem Theory*, 613 pp., Elsevier, New York, 1987.

Thompson, A. B., Fluids deep in the Earth's mantle, *Nature*, *358*, 295–302, 1992.

Toksoz, M. N., J. W. Minear, and B. R. Julian, Temperature field and geophysical effects of a downgoing slab, *J. Geophys. Res.*, *76*, 1113–1138, 1971.

Toksoz, M. N., N. H. Sleep, and A. T. Smith, Evolution of the downgoing lithosphere and the mechanisms of deep focus earthquakes, *Geophys. J. R. Astron. Soc.*, *35*, 285–310, 1973.

Tong, J., F. A. Dahlen, G. Nolet, and H. Marquering, Diffraction effects upon finite-frequency travel times: a simple 2-D example, *Geophys. Res. Lett.*, *25*, 1983–1986, 1998.

van der Hilst, R. D., Complex morphology of subducted lithosphere in the mantle beneath the Tonga trench, *Nature*, *374*, 154–157, 1995.

van der Hilst, R. D., and E. R. Engdahl, Step-wise relocation of ISC earthquake hypocenters for linearized tomographic images of slab structures, *Phys. Earth Planet. Inter.*, *75*, 39–53, 1992.

van der Hilst, R. D., and R. Snieder, High-frequency recursors to *P* wave arrivals in New Zealand: Implications for slab structure, *J. Geophys. Res.*, *101*, 8473–8488, 1996.

van der Hilst, R. D., E. R. Engdahl, W. Spakman, and G. Nolet, Tomographic imaging of subducted lithosphere below northwest Pacific island arcs, *Nature*, *353*, 37–43, 1991.

van Keken, P. E., S. Karato, and D. A. Yuen, Oceanic crust separation, *Geophys. Res. Lett.*, *23*, 1821–1824, 1996.

Vidale, J. E., Waveform effects of a high-velocity, subducted slab, *Geophys. Res. Lett.*, *14*, 541–545, 1987.

Wadati, K., On the activity of deep focus earthquakes in the Japanese Islands and neighborhood, *Geophys. Mag.*, *3*, 305–325, 1935.

Zhao, D., Y. Xu, D. A. Wiens, J. Dorman, J. Hildebrand, and S. Webb, Depth extent of the Lau back-arc spreading center and its relationship to subduction processes, *Science*, *278*, 254–257, 1997.

Zhou, H., and G. Chen, Waveform response to the morphology of 2-D subducted slabs, *Geophys. J. Int.*, *121*, 511–522, 1995.

Zhou, H., and R. W. Clayton, *P* and *S* wave travel time inversion for subducting slabs under the island arcs of the northwest Pacific, *J. Geophys. Res.*, *95*, 6829–6851, 1990.

M. Deal, Exxon Production Research Company, P.O. Box 2189, Houston, TX 77252-2189. (michael.m.deal@exxon.sprint.com)

G. Nolet, Department of Geosciences, Guyot Hall, Princeton University, Princeton, NJ 08544. (nolet@princeton.edu)

R. D. van der Hilst, Department of Earth, Atmospheric and Planetary Sciences, Room 54-514, Massachusetts Institute of Technology, Cambridge, MA 02139. (hilst@mit.edu)

(Received August 17, 1998; revised June 24, 1999;
accepted July 14, 1999.)